



# Theory and simulation of texture formation in mesophase carbon fibers

J. Yan, A.D. Rey\*

*Department of Chemical Engineering, McGill University, 3610 University St., Montreal, Quebec H3A 2B2, Canada*

Received 6 March 2002; accepted 8 May 2002

## Abstract

Carbonaceous mesophase precursors are spun into high-performance commercial carbon fibers using the standard melt spinning process. The spinning process produces a wide range of cross-sectional fiber textures whose origins are not currently well understood. The planar polar (PP) and planar radial (PR) textures are two frequently observed textures. This paper presents theory and simulations of the elasticity-driven formation process of the PP texture using the classical Landau–de Gennes mesoscopic theory for discotic liquid crystals, including defect nucleation, defect migration, and overall texture geometry. The main characteristic of the real PP texture is the presence of a pair of defects equidistant from the fiber axis. In this research it is analytically and numerically found that, under elastic isotropy, the ratio of the equilibrium defect–defect separation distance to the fiber diameter is always equal to  $1/\sqrt[4]{5}$ . The computed PP and PR textures phase diagram, given in terms of temperature and fiber radius, is used to establish the processing conditions and geometric factors that lead to the selection of these two textures.

© 2002 Published by Elsevier Science Ltd.

**Keywords:** A. Carbon fibers, Mesophase pitch; C. Modeling

## 1. Introduction

Carbonaceous mesophases, such as coal tar and petroleum pitches, are used in the industrial manufacturing of mesophase carbon fiber [1]. This relatively new carbon fiber is more competitive than the conventional fiber made from acrylic precursors in several application areas [1]. The thermodynamic phase that describes carbonaceous mesophases is the discotic nematic liquid crystal state [2]. Liquid crystals are intermediate (i.e. mesophase) phases, typically found for anisodiametric organic molecules, which exist between the higher temperature isotropic liquid state and the lower temperature crystalline state. Carbonaceous mesophases are composed of disk-like molecules. Fig. 1 shows the molecular geometry, positional disorder, and uniaxial orientational order of discotic nematic liquid crystals. The partial orientational order of the molecular unit normal  $\mathbf{u}$  is along the average orientation or director  $\mathbf{n}$  ( $\mathbf{n} \cdot \mathbf{n} = 1$ ). The name discotic dis-

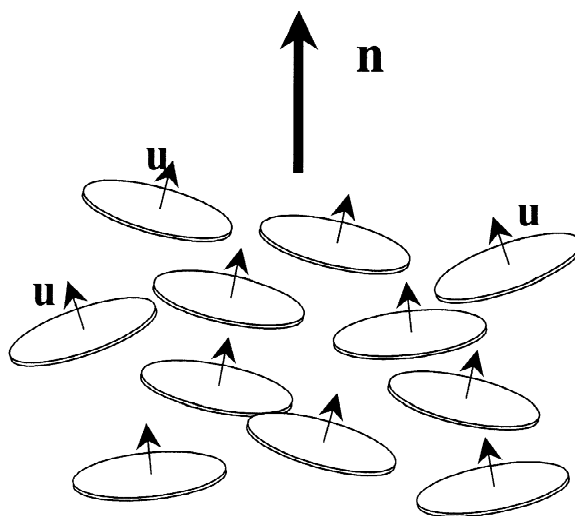


Fig. 1. Definition of director orientation of a uniaxial discotic nematic liquid crystalline material. The director  $\mathbf{n}$  is the average orientation of the unit normals to the disk-like molecules in a discotic nematic phase.

\*Corresponding author. Tel.: +1-514-398-4196; fax: +1-514-398-6678.

E-mail address: [alejandro.rey@mcgill.ca](mailto:alejandro.rey@mcgill.ca) (A.D. Rey).

tinguishes the molecular geometry and the name nematic identifies the type of liquid crystalline orientational order.

The industrial fabrication of mesophase carbon fiber using the conventional melt spinning process typically produces micrometer-sized cylindrical filaments whose cross-sectional area displays a variety of transverse textures [3], that is, different spatial arrangements of the average orientation  $\mathbf{n}$  on the plane perpendicular to the fiber axis. The selection mechanisms that drive the texture formation pattern during fiber spinning are at present not completely understood, but due to the strong structure–properties correlations, they are essential for product optimization. Significant progress in the fundamental understanding of structure formation of mesophase fibers has been presented [4,5]. The fiber structure development is the result of the application of a series of extremely complex stress and thermal fields on a complex textured anisotropic viscoelastic material. The scope of the present paper is the characterization of temperature, geometry, and elastic anisotropy effects on texture selection when elastic effects are dominant, and viscous effects are neglected. The idea behind the use of this simplifying assumption (i.e. neglectation of viscous effects) is that an understanding of elastic effects is a pre-requisite to understand the more complex viscoelastic response. In addition, if this kind of modeling shows that elastic effects produce microstructures compatible with those observed in the real world, one may then be able to conclude that viscous effects reinforce the emergence of the textures selected by elasticity.

Discotic nematic liquid crystals, such as carbonaceous mesophases, are anisotropic visco-elastic materials, whose properties depend on the average molecular orientation. As mentioned above a question of fundamental importance to the melt spinning of carbonaceous mesophases is to determine how elastic and viscous mechanisms affect the

fiber process-induced structuring and cross-sectional fiber textures' selection. When considering elastic mechanisms, it is necessary to identify the three fundamental elastic modes of these materials. Fig. 2 shows the three types of elastic deformation, splay, twist, and bend, and their corresponding modulus  $K_{11}$ ,  $K_{22}$ , and  $K_{33}$ , known as Frank elasticity constants [6]. The Frank elastic (long range) energy density  $f_n$  for uniaxial nematic liquid crystals is defined by [6]

$$f_n = \frac{K_{11}}{2}(\nabla \cdot \mathbf{n})^2 + \frac{K_{22}}{2}(\mathbf{n} \times \nabla \cdot \mathbf{n})^2 + \frac{K_{33}}{2}|\mathbf{n} \times \nabla \times \mathbf{n}|^2 \quad (1)$$

The type of liquid crystal elasticity is known as orientation elasticity and is the analogue of Hooke's elasticity of isotropic materials. In liquid crystals the strains are due to spatial orientation gradients, and are analogous to positional displacements in isotropic materials, and the Frank elastic constants play the role of Hooke's modulus of isotropic materials. The reason that there are three different constants is that the material is anisotropic, and different directions exhibit different degrees of distortions under applied loads, as in composites materials. Assuming elastic isotropy (one constant approximation),  $K = K_{11} = K_{22} = K_{33}$ , the Frank energy simplifies to [6]

$$f_n = \frac{K}{2}[(\nabla \cdot \mathbf{n})^2 + |\nabla \times \mathbf{n}|^2] \quad (2)$$

which, due to its simplicity, is widely used to perform analytical calculations [6]. We note that, in reality, for disc-like liquid crystals, the twist constant ( $K_{22}$ ) is greater than the splay ( $K_{11}$ ) and bend ( $K_{33}$ ) constants [7]:

$$K_{22} > K_{11} \quad (3a)$$

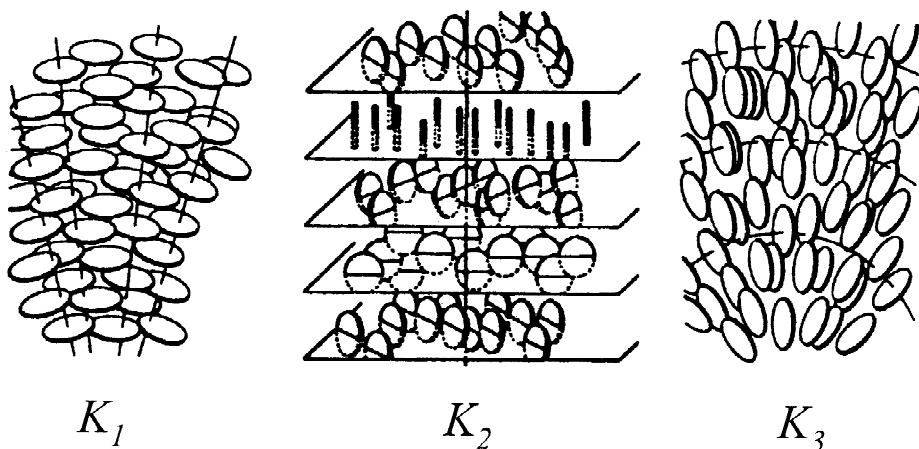


Fig. 2. Schematics of the elastic splay (left), twist (center), and bend (right) deformation for uniaxial discotic nematics. Note that the splay (bend) mode involves bending (splaying) of the disk's trajectories, in contrast to the case of uniaxial rod-like nematics. A disk trajectory is a curve locally orthogonal to the director. Adapted from Ref. [5].

$$K_{22} > K_{33} \quad (3b)$$

Note that, in contrast to rod-like nematics, for disc-like nematics the bending disc's trajectories give rise to a splay deformation, and the splaying disc's trajectories give rise to a bend deformation; by disc trajectory it means the curve locally orthogonal to the director. The Frank moduli are functions of temperature and have units of energy per unit length. Heating up a discotic mesophase above the nematic–isotropic transition temperature, it is found that  $K_{11} = K_{22} = K_{33} = 0$ , that is, the Frank elasticity is due to orientational liquid crystalline order [4].

It is known [3] that the observed cross-section fiber textures belong to a number of families, such as onion, radial, mixed, PAN-AM, to name a few. Fig. 3 shows the schematics of two cross-sectional textures most commonly seen in mesophase carbon fibers. The dashed line indicates the trajectories of the molecular planes, (a) shows the planar radial (PR) texture, in which only the pure bend mode exists with one defect in the center of strength  $+1$ , and (b) shows the planar polar (PP) texture, in which two modes of deformation, splay and bend, couple in the system with two defects of strength  $+1/2$ . The defects in these textures arise because, in a cylindrical geometry, it is impossible to tangentially align the directors at the surface without introducing singularities. Defects are singularities in the director field and are characterized by strength  $(1/2, 1, \dots)$  and sign  $(\pm)$  [6]. The strength of a disclination determines the amount of orientation distortion and the sign corresponds to the sense (i.e. clockwise or anti-clockwise) of orientation rotation while circling the defects. Since the energy of a defect scales with the square of defect strength [6], the planar polar texture would seem to emerge so as to minimize the elastic energy associated with defect distortions. In addition, defects of equal sign repel each other, while defects of different sign attract. As shown below, in the PP texture defect–defect interaction plays a critical role in the geometry of the texture.

Theory and simulation of liquid crystalline materials continues to be performed using macroscopic, mesoscopic, and molecular models [6]. Macroscopic models based on the Leslie–Ericksen director equations are unsuitable to simulate texture formation because defects are singularities in the orientation field [6]. On the other hand, mesoscopic models based on the second moment of the orientation distribution function are well suited to capture liquid crystalline textures, because defects are non-singular solutions to the governing equations. A very well established mesoscopic model in liquid crystalline materials is based on the Landau–de Gennes free energy [6] and is adopted and used in this work. Related work on fiber structure is given in [8,9].

The objectives of this paper are:

1. to simulate the transient formation of the planar polar texture that is commonly observed during the melt spinning of carbonaceous mesophase;
2. to characterize the elastic driving forces that promote the selection of the planar polar texture;
3. to provide a full geometric characterization of the planar polar textures in terms of defect locations;
4. to present and discuss the planar radial–planar polar fiber texture phase diagram, given in terms of temperature and fiber radius, and to establish the geometric and operating conditions that lead to the characteristic textures.

This paper is organized as follows. Section 2 presents the theory and the Landau–de Gennes governing equations. Section 3 presents an analytic geometric analysis of the planar polar texture that yields closed form results. Section 4 shows the numerical solutions of our model that verify the analytical predictions made in Section 3, and also discusses the characteristics of the texture evolution

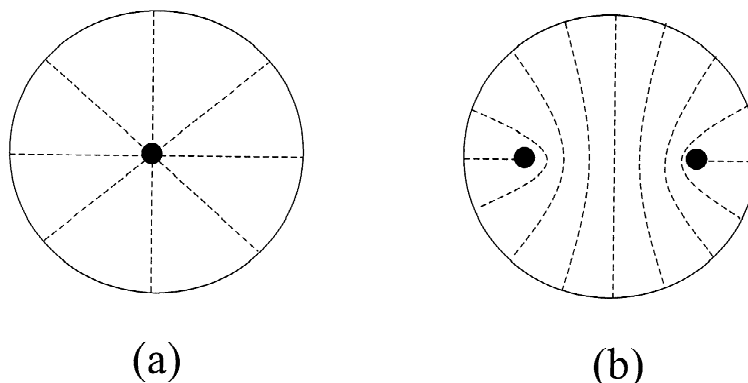


Fig. 3. Schematics of transverse textures of actual mesophase carbon fibers. (a) The planar radial (PR) texture, in which the pure bend mode ( $K_3$ ) exists with one defect in the center of strength  $+1$ . (b) The planar polar (PP) texture, in which two modes of deformation, splay ( $K_1$ ) and bend ( $K_3$ ), couple in the system with two defects of strength  $+1/2$ .

and the texture phase diagram. Finally, conclusions are presented.

## 2. Theory and governing equations

In this section, we present the Landau–de Gennes theory for nematic liquid crystals [6], and the parametric equations used to describe mesophase fiber texture formation. As mentioned above, this classical [6] liquid crystal theory is well suited to simulate texture formation since defects are non-singular solutions to the governing equations.

### 2.1. Definition of orientation and alignment

The Landau–de Gennes theory of liquid crystals [6] describes the viscoelastic behavior of nematic liquid crystals using the second moment of the orientation distribution function, known as the tensor order parameter  $\mathbf{Q}(x,t)$ , and the velocity field  $v(x,t)$ . The tensor order parameter field  $\mathbf{Q}(x,t)$  and the velocity field  $v(x,t)$  have independent origins. In the absence of macroscopic flow,  $v = 0$ , the viscoelasticity of liquid crystals is described by  $\mathbf{Q}(x,t)$ . This means that spatio-temporal changes in the order parameter may exist even in the absence of flow. In this paper macroscopic flow does not occur,  $v = 0$ , and the state of the liquid crystal is defined solely by  $\mathbf{Q}(x,t)$ . Numerous examples of viscoelastic property measurements and phenomena involving spatio-temporal changes in the absence of flow are found in the liquid crystal literature [6].

We next explain the nature, origin, and physical significance of the tensor order parameter  $\mathbf{Q}$ . To characterize the orientation in a discotic nematic liquid crystal we use the orientation distribution function (ODF)  $f(\mathbf{u})$ , which gives the probability of finding a disc unit normal  $\mathbf{u}$  with orientation between  $\mathbf{u}$  and  $\mathbf{u} + d\mathbf{u}$ . Since  $\mathbf{u}$  is a unit vector, all its possible orientations are contained in the unit sphere, denoted by  $Z^2$ . The ODF is normalized:

$$\int_{Z^2} f(\mathbf{u}) dA = 1 \quad (4)$$

Since  $\mathbf{u}$  is equivalent to  $-\mathbf{u}$ , to describe  $f(\mathbf{u})$  we must use even products:  $\mathbf{uu}, \mathbf{uuuu}, \dots$ . To expand a function  $f(\mathbf{u})$  of a unit vector  $\mathbf{u}$  we can use a Fourier series of orthogonal basis functions  $f_o, f_{ij}^2, f_{ijkl}^4, \dots$ , known as surface spherical harmonics. The products obey

$$\begin{aligned} \int_{Z^2} dA &= 4\pi, \quad \int_{Z^2} \mathbf{uu} dA = \frac{4\pi}{3} \boldsymbol{\delta}, \quad \int_{Z^2} \mathbf{uuuu} dA \\ &= \frac{4\pi}{3 \times 15} (\boldsymbol{\delta}\boldsymbol{\delta} + \mathbf{I} + \mathbf{I}^+), \dots \end{aligned} \quad (5)$$

where  $(\boldsymbol{\delta}\boldsymbol{\delta})_{mnpq} = \delta_{mn}\delta_{pq}$ ,  $\mathbf{I}_{mnpq} = \delta_{mq}\delta_{np}$ , and  $\mathbf{I}^+ = \delta_{mp}\delta_{nq}$ , which are used in expanding  $f(\mathbf{u})$ . The surface spherical

harmonics are orthogonal completely symmetric surface tensors, given by

$$\begin{aligned} f_o &= 1, \quad f_{ij}^2 = u_i u_j - \frac{\delta_{ij}}{3}, \quad f_{ijkl}^4 \\ &= u_i u_j u_k u_l - \frac{1}{7} \{ \delta_{ij} u_k u_l + \delta_{ik} u_j u_l + \delta_{il} u_j u_k + \delta_{jk} u_i u_l \\ &\quad + \delta_{jl} u_i u_k \} + \frac{1}{5 \times 7} \{ \delta_{ij} \delta_{kl} + \delta_{ik} \delta_{jl} + \delta_{il} \delta_{jk} \} \end{aligned} \quad (6)$$

Expanding  $f(\mathbf{u})$  as a Fourier series:

$$\begin{aligned} f(\mathbf{u}) &= \frac{1}{4\pi} 1 \cdot f_o + \frac{3 \times 5}{4\pi \times 2} \mathbf{Q}_{ij}^2 f_{ij}^2 + \frac{3 \times 5 \times 7 \times 9}{4\pi \times 2 \times 3 \times 4} \mathbf{Q}_{ij}^4 f_{ij}^4 \\ &\quad + \dots \end{aligned} \quad (7)$$

where the coefficients of the Fourier expansion,  $\mathbf{Q}^2, \mathbf{Q}^4, \dots$  are symmetric and traceless tensors, and where the numerical coefficients  $(1/4\pi, \dots)$  are used to normalize the  $\mathbf{Q}$ 's. The coefficients are found using the principle of orthogonality, as used in any Fourier series expansion. For example, to find  $\mathbf{Q}^2$  we dot  $f(\mathbf{u})$  with  $f^2$  to obtain

$$\begin{aligned} \mathbf{Q} \equiv \mathbf{Q}^2 &= \int_{Z^2} f(\mathbf{u}) f^2 dA = \int_{Z^2} f(\mathbf{u}) \left( \mathbf{uu} - \frac{\boldsymbol{\delta}}{3} \right) dA \\ &= \left\langle \mathbf{uu} - \frac{\boldsymbol{\delta}}{3} \right\rangle \end{aligned} \quad (8)$$

where for simplicity we define  $\mathbf{Q} \equiv \mathbf{Q}^2$ . In the Landau–de Gennes theory the description of the nematic microstructure is limited to the second-order term  $\mathbf{Q}$ , while the higher-order terms are neglected. Thus this theory contains an approximation since information residing in higher-order terms is not accounted for.

The second-order symmetric and traceless tensor order parameter  $\mathbf{Q}$  [6] is efficiently expressed as

$$\mathbf{Q} = S(\mathbf{nn} - \frac{1}{3}\boldsymbol{\delta}) + \frac{1}{3}\mathbf{P}(\mathbf{mm} - \mathbf{ll}) \quad (9a)$$

where the following restrictions apply

$$\mathbf{Q} = \mathbf{Q}^T \quad (9b)$$

$$\text{tr}(\mathbf{Q}) = 0 \quad (9c)$$

$$-\frac{1}{2} \leq S \leq 1 \quad (9d)$$

$$-\frac{3}{2} \leq P \leq \frac{3}{2} \quad (9e)$$

$$\mathbf{n} \cdot \mathbf{n} = \mathbf{m} \cdot \mathbf{m} = \mathbf{l} \cdot \mathbf{l} = 1 \quad (9f)$$

$$\mathbf{nn} + \mathbf{mm} + \mathbf{ll} = \boldsymbol{\delta} = \begin{bmatrix} 1 & 0 & 0 \\ 0 & 1 & 0 \\ 0 & 0 & 1 \end{bmatrix} \quad (9g)$$

Equivalently, the symmetric traceless tensor order parameter  $\mathbf{Q}$  can be written as an expansion of its eigenvectors:

$$\mathbf{Q} = \mu_n \mathbf{nn} + \mu_m \mathbf{mm} + \mu_l \mathbf{ll} \quad (10a)$$

$$\mu_n + \mu_m + \mu_l = 0 \quad (10b)$$

where the uniaxial director  $\mathbf{n}$  corresponds to the maximum eigenvalue  $\mu_n = \frac{2}{3}S$ , the biaxial director  $\mathbf{m}$  corresponds to the second largest eigenvalue  $\mu_m = -\frac{1}{3}(S - P)$ , and the second biaxial director  $\mathbf{l} (= \mathbf{n} \times \mathbf{m})$  corresponds to the smallest eigenvalue  $\mu_l = -\frac{1}{3}(S + P)$ . The orientation is defined completely by the orthogonal director triad  $(\mathbf{n}, \mathbf{m}, \mathbf{l})$ . The magnitude of the uniaxial scalar order parameter  $S$  is the molecular alignment along the uniaxial director  $\mathbf{n}$ , and is given by  $S = \frac{2}{3}(\mathbf{n} \cdot \mathbf{Q} \cdot \mathbf{n})$ . The magnitude of the biaxial scalar order parameter  $P$  is the molecular alignment in a plane perpendicular to the direction of the uniaxial director  $\mathbf{n}$ , and is given by  $P = \frac{3}{2}(\mathbf{m} \cdot \mathbf{Q} \cdot \mathbf{m} - \mathbf{l} \cdot \mathbf{Q} \cdot \mathbf{l})$ . On the principal axes, the tensor order parameter  $\mathbf{Q}$  is represented as

$$\mathbf{Q} = \begin{bmatrix} -\frac{1}{3}(S - P) & 0 & 0 \\ 0 & -\frac{1}{3}(S + P) & 0 \\ 0 & 0 & \frac{2}{3}S \end{bmatrix} \quad (11)$$

where both  $S$  and  $P$  are positive for normal disc-like uniaxial nematic liquid crystals.

The Landau–de Gennes model uses the tensor order parameter to describe nematic ordering. According to Eq. (11), the model is able to describe biaxial ( $S \neq 0, P \neq 0$ ), uniaxial ( $S \neq 0, P = 0$ ), and isotropic ( $S = 0, P = 0$ ) states. The isotropic state is the zero tensor:  $\mathbf{Q} = 0$ . Defects are regions of molecular size in which orientational order ( $S, P$ ) sharply decrease. These localized disordered regions are in principle captured by mesoscopic models since  $\mathbf{Q}$  remains well behaved.

## 2.2. Landau–de Gennes mesoscopic model for liquid crystalline materials

According to the Landau–de Gennes model, the bulk energy density of nematic liquid crystals (NLC) in the absence of external fields is given by [10]

$$f_b = f_s + f_l \quad (12)$$

where  $f_s$  is the short-range energy density, which is responsible for the nematic–isotropic phase transition, and  $f_l$  is the elastic free energy density [6], which contains long-range gradient contributions to the system. The dimensionless free energy densities  $f_s$  and  $f_l$  of thermotropic liquid crystals, in terms of the second-order tensor  $\mathbf{Q}$ , are given by

$$f_s = \frac{3}{U} \left( \frac{1}{2} \left( 1 - \frac{1}{3}U \right) \mathbf{Q} \cdot \mathbf{Q} - \frac{1}{3}U \mathbf{Q} \cdot (\mathbf{Q} \cdot \mathbf{Q}) + \frac{1}{4}U (\mathbf{Q} \cdot \mathbf{Q})^2 \right) \quad (13a)$$

$$f_l = \frac{L_1}{2ckT^*} [\nabla \mathbf{Q} \cdot (\nabla \mathbf{Q})^T] + \frac{L_2}{2ckT^*} (\nabla \cdot \mathbf{Q}) \cdot (\nabla \cdot \mathbf{Q}) \quad (13b)$$

where  $U$  is the nematic potential, which is related to the temperature in a thermotropic liquid crystal, and  $c, k, T^*$  are the number density of the discs, the Boltzmann's constant, and an absolute reference temperature just below the isotropic–nematic phase transition temperature, respectively. The bare elastic constants  $L_1$  and  $L_2$  are known as Landau coefficients. To relate the Landau coefficients appearing in Eq. (8) to the previously defined Frank elastic constants for uniaxial liquid crystals appearing in Eq. (1), we restrict the tensor order parameter  $\mathbf{Q}$  to its uniaxial form  $\mathbf{Q} = S_{eq}(\mathbf{nn} - \mathbf{I}/3)$  with  $S$  equal to its equilibrium spatially homogeneous value  $S_{eq}$  (see Eq. (22)). In the uniaxial state, Eq. (13b) then becomes

$$f_n = S_{eq}^2 \left\{ (L_1 + \frac{1}{2}L_2)(\nabla \cdot \mathbf{n})^2 + L_1(\mathbf{n} \times \nabla \cdot \mathbf{n})^2 + (L_1 + \frac{1}{2}L_2)|\mathbf{n} \times \nabla \times \mathbf{n}|^2 \right\} \quad (14)$$

Comparing equal terms in Eqs. (1) and (14) the relations between  $L_1$  and  $L_2$  and the Frank's constants of uniaxial LCs are [13]

$$L_1 = \frac{K_2}{2S_{eq}^2} \quad (15a)$$

$$L_2 = \frac{K - K_2}{S_{eq}^2} \quad (15b)$$

The Landau coefficients  $L_1$  and  $L_2$  are bare elastic constants, independent of temperature. On the other hand, the Frank elastic constants are temperature dependent, since the scalar order parameter  $S$  is a function of temperature [6]. Eq. (14) implies that, when using Eq. (13b), the elastic anisotropy restrictions  $K = K_1 = K_3 \neq K_2$  apply. Thermodynamic stability restrictions impose the following inequalities [11]:

$$L_1 > 0 \quad (16a)$$

$$3L_1 + 5L_2 > 0 \quad (16b)$$

In addition, the molecular disc-like geometry involved in the discotic nematic phase requires that [12]

$$L_2 < 0 \quad (17)$$

Using the classical relaxation of free energy model, the time-dependent equation in terms of  $\mathbf{Q}$  and  $\nabla \mathbf{Q}$  is found to be [14]

$$-\gamma(\mathbf{Q}) \frac{d\mathbf{Q}}{dt} = \left[ \frac{\delta F}{\delta \mathbf{Q}} \right]^{[s]} = \left( \frac{\partial f_s}{\partial \mathbf{Q}} - \nabla \cdot \frac{\partial f_l}{\partial \nabla \mathbf{Q}} \right)^{[s]} \quad (18)$$

where [s] indicates symmetric and traceless,  $\gamma(\mathbf{Q})$  is a phenomenological kinetic coefficient, and  $\delta F/\delta \mathbf{Q}$  is the functional derivative of the total energy  $F$ . Eq. (18) is five coupled non-linear parabolic reaction-diffusion equations for the five independent components of  $\mathbf{Q}$ :  $Q_{xx}, Q_{yy}, Q_{xy}, Q_{xz}, Q_{yz}$ . Substituting Eq. (13) into Eq. (18) yields the following governing equations of  $\mathbf{Q}(x, t)$  [10]:

$$\begin{aligned} \frac{d\mathbf{Q}}{dt} = & -6\overline{Dr} \frac{3}{U} \left[ \left(1 - \frac{1}{3}U\right) \mathbf{Q} - U \left( \mathbf{Q} \cdot \mathbf{Q} - \frac{1}{3}(\mathbf{Q} \cdot \mathbf{Q}) \mathbf{I} \right) \right. \\ & + U(\mathbf{Q} \cdot \mathbf{Q}) \mathbf{Q} \left. \right] + 6\overline{Dr} \left[ \frac{L_1}{ckT^*} \nabla^2 \mathbf{Q} \right. \\ & + \frac{L_2}{2ckT^*} \left( \nabla (\nabla \cdot \mathbf{Q}) + [\nabla (\nabla \cdot \mathbf{Q})]^T \right. \\ & \left. \left. - \frac{2}{3} \text{tr}[\nabla (\nabla \cdot \mathbf{Q})] \mathbf{I} \right) \right] \end{aligned} \quad (19a)$$

$$\overline{Dr} \approx Dr \frac{1}{(1 - (3/2)\mathbf{Q} \cdot \mathbf{Q})^2} \quad (19b)$$

$$Dr = \frac{ckT}{6\eta} \quad (19c)$$

where  $\overline{Dr}$  is the microstructure-dependent rotational diffusivity,  $D_r$  is the preaveraged rotational diffusivity or isotropic diffusivity, which is independent of  $\mathbf{Q}$ , and  $\eta$  is viscosity. Non-dimensioning Eq. (19) yields [10]

$$\begin{aligned} \frac{d\mathbf{Q}}{dt^*} = & -\frac{1}{U} \frac{3}{U} \left[ 1 - \frac{3}{2}(\mathbf{Q} \cdot \mathbf{Q}) \right]^{-2} \left[ \left(1 - \frac{1}{3}U\right) \mathbf{Q} \right. \\ & - U \left( \mathbf{Q} \cdot \mathbf{Q} - \frac{1}{3}(\mathbf{Q} \cdot \mathbf{Q}) \mathbf{I} \right) + U(\mathbf{Q} \cdot \mathbf{Q}) \mathbf{Q} \left. \right] \\ & + \frac{\xi^2}{R^2} \frac{1}{U} \left[ 1 - \frac{3}{2}(\mathbf{Q} \cdot \mathbf{Q}) \right]^{-2} \left\{ \nabla^2 \mathbf{Q} \right. \\ & + \frac{\tilde{L}_2}{2} \left[ \tilde{\nabla} (\tilde{\nabla} \cdot \mathbf{Q}) + [\tilde{\nabla} (\tilde{\nabla} \cdot \mathbf{Q})]^T \right. \\ & \left. \left. - \frac{2}{3} \text{tr}[\tilde{\nabla} (\tilde{\nabla} \cdot \mathbf{Q})] \mathbf{I} \right] \right\} \end{aligned} \quad (20)$$

To facilitate the discussion, we define

$$\begin{aligned} \mathbf{Z} = & -\frac{1}{U} \frac{3}{U} \left[ 1 - \frac{3}{2}(\mathbf{Q} \cdot \mathbf{Q}) \right]^{-2} \left[ \left(1 - \frac{1}{3}U\right) \mathbf{Q} \right. \\ & - U \left( \mathbf{Q} \cdot \mathbf{Q} - \frac{1}{3}(\mathbf{Q} \cdot \mathbf{Q}) \mathbf{I} \right) + U(\mathbf{Q} \cdot \mathbf{Q}) \mathbf{Q} \left. \right] \end{aligned} \quad (21a)$$

$$\begin{aligned} \mathbf{L} = & \frac{\xi^2}{R^2} \frac{1}{U} \left[ 1 - \frac{3}{2}(\mathbf{Q} \cdot \mathbf{Q}) \right]^{-2} \left\{ \nabla^2 \mathbf{Q} \right. \\ & + \frac{\tilde{L}_2}{2} \left[ \tilde{\nabla} (\tilde{\nabla} \cdot \mathbf{Q}) + [\tilde{\nabla} (\tilde{\nabla} \cdot \mathbf{Q})]^T \right. \\ & \left. \left. - \frac{2}{3} \text{tr}[\tilde{\nabla} (\tilde{\nabla} \cdot \mathbf{Q})] \mathbf{I} \right] \right\} \end{aligned} \quad (21b)$$

$$\frac{d\mathbf{Q}}{dt^*} = \mathbf{Z} + \mathbf{L} \quad (21c)$$

where  $t^* = t(3ckT^*/\eta)$  is dimensionless time,  $U = 3T^*/T$  is dimensionless temperature,  $\xi = (L_1/ckT^*)^{1/2}$  is the

coherence length (defect core size) [4],  $\tilde{L}_2 = L_2/L_1$  is the dimensionless elastic coefficient,  $R$  is the geometry length scale (i.e. the fiber radius),  $\mathbf{Z}$  is the short-range contribution, and  $\mathbf{L}$  is the long-range distribution. The coherence length has units of length [6], and is the internal length scale of the material that arises due to the short-range energy. The coherence length  $\xi$  is the defect core radius. In a model with no short-range energy defect cores cannot be described. This is the reason why the Landau–de Gennes theory is widely used to describe defect nucleation processes [10]. In the Landau–de Gennes model the tensor order parameter is defined all the way up to, and including, the center of the defect core, as discussed below in conjunction with Eq. (41). The energy of the defect core is found by integrating the total energy density (see Fig. 6e for an example of the total long-range density as a function of time, which captures the splitting of an  $s = +1$  defect into two  $s = +1/2$  defects).

Here we discuss the main effects arising from  $\mathbf{Z}$  and  $\mathbf{L}$  (see Eq. (21)). As mentioned above,  $\mathbf{Z}$  represents the short-range elastic contribution, which governs the isotropic–nematic phase transition and tends to keep the molecular order ( $S, P$ ) equal to that of the equilibrium state in a local domain. The second term  $\mathbf{L}$  is the long-range order elastic effect of the molecular field to impose an energetic penalty for any spatial gradients ( $\nabla \mathbf{Q} \neq 0$ ). As mentioned before, the long-range effect is known as the Frank elasticity. The dimensionless parameters of the model, which arise in Eq. (20), are  $U$ ,  $\Psi = R/\xi$ , and  $\tilde{L}_2$ . The nematic potential  $U$  is a dimensionless temperature that controls the equilibrium order parameter  $S_{eq}$  at the phase transition. According to the Doi–Edwards uniaxial nematic theory [14]:

$$S_{eq} = \frac{1}{4} + \frac{3}{4} \sqrt{1 - \frac{8}{3U}} \quad (22a)$$

$$U = \frac{3T^*}{T} \quad (22b)$$

where  $T^*$  is an absolute reference temperature just below the isotropic–nematic phase transition temperature as defined before. For  $U < 8/3$  the stable phase is isotropic, for  $8/3 \leq U \leq 3$  there is biphasic equilibrium, and for higher values of  $U$  the phase is uniaxial nematic. In this work, we have used  $2.8 \leq U \leq 6.55$ . The parameter  $\Psi = R/\xi$  is the ratio of the fiber radius ( $R$ ) to the coherence length scale ( $\xi$ ). As mentioned above, the coherence length represents the characteristic size of a defect core and for micron-sized carbon fibers at typical processing temperatures (300 °C), it is usually much smaller than the system size  $R$ . In this work, we have used  $0 < \Psi < 150$ . When  $\Psi \ll 1$ , long-range energy dominates, spatial gradients are costly and homogeneous states are selected. On the other hand, when  $\Psi \gg 1$ , long-range elasticity is insignificant with respect to short-range elasticity and defects may proliferate, since spatially, non-homogeneous

states are energetically not costly. The dimensionless scale  $\tilde{L}_2 = L_2/L_1$  is a measurement of elastic anisotropy. When  $\tilde{L}_2 = 0$ , the system is isotropic and the splay, bend, and twist elastic modes have the same elastic modulus. The thermodynamic restrictions (Eq. (16)) yield [11]

$$\tilde{L}_2 > -\frac{3}{5} \quad (23)$$

In addition, since for discotic nematics inequalities (3a,b) hold, we further restrict  $\tilde{L}_2$  as

$$-\frac{3}{5} < \tilde{L}_2 \leq 0 \quad (24)$$

In this paper, we have used  $\tilde{L}_2 = -0.5$  throughout.

Since we are modelling mesophase fiber of circular cross-section the selected computational domain must be circular. As mentioned above, flow is absent ( $v = 0$ ) and the fiber's cross section is always circular, since it is initially circular; as mentioned above, the tensor order parameter is independent of the velocity even under spatio-temporal changes. The governing Eq. (20) is solved in a circle of dimensionless radius  $\tilde{r} = 1/2$ , with the following boundary conditions:

$$t^* > 0, \quad \tilde{r} = 1/2, \quad \mathbf{Q} = \mathbf{Q}_o \quad (25a)$$

$$\mathbf{Q}_o = S_{eq}(\alpha\alpha - \frac{1}{3}\mathbf{I}) \quad (25b)$$

The symbol  $\tilde{r}$  is the dimensionless radial distance ( $\tilde{r} = r/R$ ), and  $\tilde{r} = 0$  is the center of the computational domain (i.e. fiber axis). The Dirichlet boundary condition (20) sets the eigenvalues of the uniaxial tensor order parameter equal to its equilibrium value ( $S = S_{eq}$ ), and the distinct eigenvector  $\mathbf{n}$  parallel to the azimuthal ( $\alpha$ ) direction of the cylindrical coordinates system ( $\tilde{r}, \alpha$ ). The symbol  $\alpha$  represents the unit vector along the azimuthal  $\alpha$  direction. The boundary condition (20) restricts  $\mathbf{Q}$  to be uniaxial ( $P = 0$ ) with its unique eigenvector  $\mathbf{n}$  along the azimuthal direction  $\alpha$ . Since the actual fiber textures [3] we wish to simulate have a director orientation  $\mathbf{n}$  parallel to  $\alpha$ , we impose this orientation to capture reality. Since the actual fiber textures do not show any significant biaxiality we restrict the tensor order parameter  $\mathbf{Q}$  to its uniaxial state ( $P = 0$ ). Biaxiality only plays a minor role in the defect core region. Far from the defect core the tensor order parameter is uniaxial because the disc-like molecules are uniaxial and the homogeneous equilibrium state is therefore uniaxial (see Eq. (22a) and Ref. [6]). Boundary condition (25) is known in the liquid crystal literature as a strong anchoring condition [6]. The tensor order parameter at a free surface or an interface depends on the chemo-mechanical interactions of the liquid crystal and the surrounding material. The free surface (or interfacial) free energy density of a liquid crystal surface (or interface) is given by [15,16]

$$\gamma = \gamma_{iso} + \frac{\gamma_{an}}{2}(\mathbf{Q} - \mathbf{Q}_o)^2 \quad (26)$$

where  $\gamma_{iso}$  is the isotropic ( $\mathbf{Q}$ -independent) contribution

and the second term is the  $\mathbf{Q}$ -dependent anisotropic contribution. The symbol  $\gamma_{an}$  represent the anchoring coefficient and  $\mathbf{Q}_o$  is the preferred order parameter that minimizes the surface energy. The extrapolation length  $EL$  is the ratio of the characteristic bulk elastic energy ( $L_1$ ) and the surface anchoring energy ( $\gamma_{an}$ ) [6]:

$$EL = \frac{L_1}{\gamma_{an}} \quad (27)$$

and has units of length since  $L_1$  has units of energy/length and  $\gamma_{an}$  of energy/area. The extrapolation length is an interfacial intrinsic length scale that may be larger, equal, or smaller than the characteristic system size, which in our case is the fiber radius  $R$ . For a given shape, when the system size  $R$  is much larger than the extrapolation length  $EL$  the minimization of the total (bulk + surface) energy is achieved by introducing less costly bulk distortions and minimizing the more costly surface energy. In this case the tensor order parameter at the surface  $\mathbf{Q}_s$  is always equal to the preferred tensor order parameter  $\mathbf{Q}_o$ :  $\mathbf{Q}_s = \mathbf{Q}_o$ . Typically,  $EL$  is in the nanometer scale and thus for the mesophase fibers of interest in this paper the surface energy is always minimized and  $\mathbf{Q}_s = \mathbf{Q}_o$ . Since we are modelling a real material fiber with known and fixed surface director orientation along the azimuthal direction we adopt boundary condition (25). To complete the discussion on boundary conditions for liquid crystalline materials we note that, when the fiber radius  $R$  is much smaller than the extrapolation length  $LE$ , the more costly bulk energy is minimized by adopting a spatially homogeneous tensor order parameter and storing less costly surface energy by introducing deviations of the surface tensor order parameter  $\mathbf{Q}_s$  from the preferred value  $\mathbf{Q}_o$ ; in this case  $\mathbf{Q}_s \neq \mathbf{Q}_o$ .

The initial conditions are

$$t^* = 0, \quad \mathbf{Q}_{ini} = S_{ini}(\mathbf{n}_{ini}\mathbf{n}_{ini} - \frac{1}{3}\mathbf{I}) + \frac{1}{3}P_{ini}(\mathbf{m}_{ini}\mathbf{m}_{ini} - \mathbf{l}_{ini}\mathbf{l}_{ini}) \quad (28)$$

where  $S_{ini}$  and  $P_{ini}$  are random and  $S_{ini} \approx 0$ ,  $P_{ini} \approx 0$ , and  $\mathbf{n}_{ini}$ ,  $\mathbf{m}_{ini}$ , and  $\mathbf{l}_{ini}$  are the three corresponding random eigenvectors. The initial conditions represent an isotropic state ( $S = 0$ ,  $P = 0$ ) with thermal fluctuations in order ( $S, P$ ) and orientation ( $\mathbf{n}, \mathbf{m}, \mathbf{l}$ ). The initial conditions are spatially inhomogeneous, since at each mesh point the amplitudes ( $S, P$ ) and the phases ( $\mathbf{n}, \mathbf{m}, \mathbf{l}$ ) of  $\mathbf{Q}$  are randomly selected.

### 3. Geometric analysis for planar polar textures

In this section, we present a geometric analysis of the planar polar texture, with the objective of deriving an expression for the distance  $d$  between the two  $s = +1/2$  disclinations. The analytical results for the defect separation distance  $d$  of this section will be compared with the numerical results obtained by solving the full model (Eq. (20)). The comparison will be presented in Section 4. It

will be shown that the analytical and numerical results are in perfect agreement with each other. The close form analytical results for the defect separation distance provide insight into the planar polar texture structure and, equally important, they also provide a consistency check for the numerical results. The director field of the planar polar texture cannot be obtained analytically, and a numerical solution to the full Eq. (20) is necessary.

To find a close form expression for  $d$ , we must assume isotropic elasticity,  $\tilde{L}_2 = 0$ , and uniaxiality (i.e.  $P = 0$ ). The director  $\mathbf{n}$  orientation in the PP texture is best analyzed using a polar cylindrical coordinate system  $(r, \alpha)$ . To satisfy the unit length restriction ( $\mathbf{n} \cdot \mathbf{n} = 1$ ), we parameterize the director as follows:

$$\begin{aligned} n_r &= \cos \theta(\alpha) \\ n_\alpha &= \sin \theta(\alpha) \end{aligned} \quad (29)$$

assuming that, outside the defect cores, the scalar order parameter is constant and equal to its equilibrium value,  $S = S_{eq}$  (see Eq. (22)). The long-range free energy density then becomes

$$f_1 = \frac{K}{2} (\nabla \theta)^2 \quad (30)$$

where we have used Eqs. (14) and (15). Replacing this last equation in the governing equation (20), assuming steady state, we obtain the classical Laplace's equation of orientation elasticity that governs the steady planar (2-D) director field of a nematic liquid crystal in any geometry [6]:

$$\nabla^2 \theta = 0 \quad (31)$$

A general singular defect solution of the Laplace equation in polar  $(r, \alpha)$  coordinates to the director angle  $\theta$  is [6]

$$\theta(\alpha) = s\alpha + c \quad (32)$$

where  $c$  is an arbitrary constant and  $s$  is the strength of the defect. This singular solution is independent of the radial coordinate [6]. These singular defect solutions are known as wedge disclination lines and are always observed in nematic liquid crystals [6]. The name nematic means thread and refers to the disclination lines observed under cross polars [6]. Since the director orientation angle  $\theta$  is governed by the linear Laplace operator ( $\nabla^2$ ), the principle of superposition can be used to describe textures with two or more defects. The general solution to the Laplace equation in the presence of an arbitrary number  $n$  of defects of strength  $s_i$ , at a point N, is [6]

$$\theta = \sum_{i=1}^n s_i \alpha_i + c \quad (33)$$

where  $\alpha_i$  is the polar angle of the ray originating at the defect of strength  $s_i$  and ending at point N,  $c$  is a constant and  $\theta$  is the director angle at point N. For the planar polar

texture studied in this paper (see Fig. 3b), with two defects of equal strength  $s = +1/2$ , the director field is

$$\theta = \frac{1}{2}(\alpha_1 + \alpha_2) + c \quad (34)$$

This director field describes the orientation state that is independent of the radial coordinate in the absence of any boundaries. Since in the PP texture the director is a function of the radial coordinate, Eq. (34) is not a solution to the PP texture. As mentioned above, since there is no analytical solution to the planar polar texture, numerical solutions (presented in Section 4) to the governing equations are necessary.

Next, we use the generally valid Eq. (32) to analyze the planar polar texture for a fiber of radius  $R$ . Fig. 4a shows a schematic of the fiber cross-section, and the coordinate

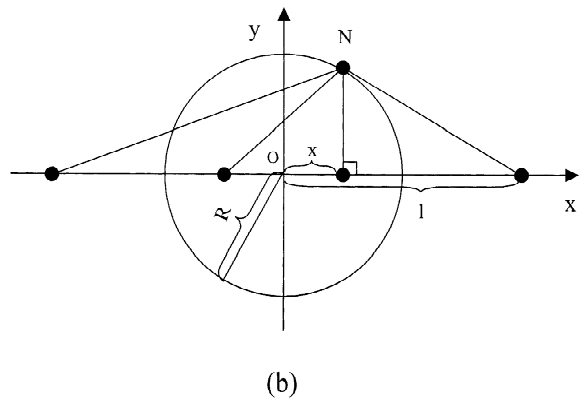
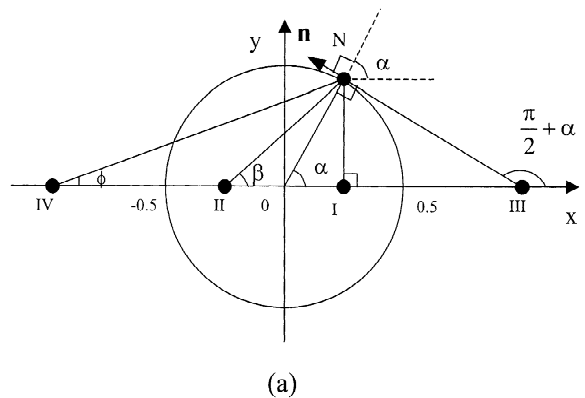


Fig. 4. Schematic of fiber geometry. (a) The dots I and II are two defects of strength  $s = +1/2$  in the computational domain and III and IV are two image defects of strength  $s = +1/2$ . P is an arbitrary point on the surface, on which the director  $\mathbf{n}$  is tangential to the surface. (b) The distance between defect and coordinate origin is  $x$ , the distance between image and coordinate origin is  $\ell$ , and the fiber radius is  $R$ .



system. The dots denoted I and II are the two disclination lines of strength  $s = +1/2$  parallel to the fiber texture axis. The  $x$ -axis is defined by  $\alpha = 0$  in our polar coordinates. The geometric analysis consists of finding the dimensionless distance  $d^*$  between two defects that minimizes the long-range energy. According to Fig. 3b, the director angle at the fiber surface is tangential. Thus at any arbitrary point N on the surface, the director angle  $\theta$  measured with respect to the  $x$ -axis is

$$\theta = \frac{\pi}{2} + \alpha \quad (35)$$

Since Eq. (34) describes the director angle for a two defects texture without constraints, the effect of fixed boundary conditions given by Eq. (35) needs to be incorporated. A multiple defects solution in the presence of boundary constraints is best obtained using the method of images in which a surface orientation constraint is captured by an image defect. The method of images is widely used to obtain analytical defect solutions in liquid crystalline materials, and full details can be found in the literature [6]. Fig. 4a shows the two image defects, denoted III and IV, for this particular problem. The strength  $s$  of the two image defects is again  $+1/2$ . We locate the two image defects at a distance  $\ell$  from the fiber axis such that the director boundary condition is tangential (see Eq. (36)). Using Eq. (33) to take into account the contribution from the two defects, we find that the director orientation at an arbitrary point N lying on the fiber surface is

$$\begin{aligned} \theta_N &= \frac{\pi}{2} + \alpha \\ &= s\left(\frac{\pi}{2}\right) + s(\beta) + s(\phi) + s\left(\frac{\pi}{2} + \alpha\right) + c \end{aligned} \quad (36)$$

where  $\alpha$ ,  $\beta$  and  $\phi$  are defined in Fig. 4a, and where  $c$  is an arbitrary constant. Eq. (31) states that the superposition of the four defect (I, II, III, IV) solutions satisfies the tangential boundary condition given by Eq. (35). Fig. 4b shows how the defect and image distances are related to the fiber axis. The two defects (I, II) are located at a distance  $\pm x$  from the fiber axis and the two images (III, IV) are located at a distance  $\pm \ell$  from the fiber axis. It turns out that to find  $x$  and define the geometry of the PP texture,  $\ell$  must also be known. In our case,  $s = +1/2$ ,  $c = 0$ , and Eq. (36) then becomes

$$\alpha = \phi + \beta \quad (37)$$

According to Eq. (37), the relation between the angular coordinates is

$$\tan \alpha = \tan(\phi + \beta) = \frac{\tan \phi + \tan \beta}{1 - \tan \phi \cdot \tan \beta} \quad (38)$$

Using Eq. (38) in conjunction with the following trigonometric relations:

$$\begin{aligned} \tan \phi &= \frac{R \sin \alpha}{\ell + x} \\ \tan \alpha &= \frac{R \sin \alpha}{x} \\ \tan \beta &= \frac{R \sin \alpha}{2x} \\ \sin^2 \alpha + \cos^2 \alpha &= 1 \\ \cos \alpha &= \frac{x}{R} \end{aligned} \quad (39a)$$

we finally get

$$xR = \ell^2 \quad (39b)$$

which relates the fiber radius  $R$  to the defect distance  $x$ , and image position  $\ell$ . Since  $\ell$  is unknown, another equation is needed. The additional equation needed to find  $\ell(x)$  is the defect–defect force balance equation. We next discuss defect–defect interactions in nematic liquid crystals following the classical treatment [6]. The energy per unit length of an isolated wedge disclination of strength  $s$  in a circular layer of radius  $R$  is given by [6]

$$f_1 = \frac{K}{2} (\nabla \theta)^2 \quad (40a)$$

$$W = W_c + \int_0^{2\pi} d\alpha \int_{r_c}^R f_1 r dr = W_c + \pi K s^2 \ln\left(\frac{R}{r_c}\right) \quad (40b)$$

where  $r_c$  is a cut-off radius of molecular size, and  $W_c$  is the core energy. As  $R \rightarrow \infty$  the energy diverges,  $W \rightarrow \infty$ , logarithmically. Since  $W$  scales with  $s^2$ , defects of strength greater than  $\pm 1/2$  will tend to dissociate into  $\pm 1/2$  defects. Following the previous single-defect energy calculation procedure (Eqs. (40a) and (40b)), the energy per unit length  $W$  associated with two defects of strength  $s_1$  and  $s_2$ , separated by a distance  $r_{12}$ , is readily found [6]:

$$\begin{aligned} W &= W_c + \int_0^{2\pi} d\alpha \int_{r_c}^R f_1 r dr \\ &= W_c + \pi K (s_1 + s_2)^2 \ln\left(\frac{R}{r_c}\right) - 2\pi K s_1 s_2 \ln\left(\frac{r_{12}}{2r_c}\right) \end{aligned} \quad (41)$$

where  $r_c \ll r_{12} < R$ . Then the interaction force  $F_{12}$  per unit length between two defects is [6]

$$F_{12} = -\frac{dW}{dr_{12}} = 2\pi K \frac{s_1 s_2}{r_{12}}, \quad r_{12} \gg r_c \quad (42)$$

which shows that the force  $F_{12}$  is inversely proportional to their separation distance  $r_{12}$ , and that defect pairs of like sign repel and defect pairs of the same sign attract. Note that the interaction force is valid when the defect separation distance is macroscopic. For length scales of the order of the core size ( $r_c$ ) numerical integration of the full Eq. (20) is necessary, since at the core the eigenvalues of

$\mathbf{Q}$  vary (see Fig. 5). In the case of  $2s = +1/2$  defects separated by a distance  $2x$  the repulsion force between the two defects is

$$F_{12} = \frac{\pi K}{x} \quad (43)$$

We can now calculate the total force per unit length exerted on defect I by the presence of: (a) a defect (II) of strength  $s = +1/2$  at a distance  $2x$ , (b) an image defect of strength  $+1/2$  at a distance  $\ell - x$  (III) and (c) another image defect of strength  $+1/2$  at a distance  $\ell + x$  (IV), as shown in Fig. 4b. All forces are repulsive because all the defects and images are of the same type:  $s = +1/2$ . The repulsive force between I and III is to the left in the selected coordinate system (see Fig. 4) and the repulsive forces between I and II, and between I and IV to the right (see Fig. 4). Employing Eq. (42), the force balance on defect I exerted by II, III and IV is

$$\frac{1}{\ell - x} = \frac{1}{2x} + \frac{1}{\ell + x} \quad (44)$$

Coupling Eqs. (39b) and (44) we finally obtain the following defect distance equation:

$$x = \frac{1}{\sqrt[4]{5}} R \quad (45)$$

which means that when the system reaches steady state, the two defects lie on a circle of radius  $1/\sqrt[4]{5}R$ . Eq. (45) is one of the main results of this paper and will be validated (see Section 4 and Figs. 8 and 9) by the numerical integration of Eq. (20). In the absence of elastic anisotropy ( $L_2 = 0$ ), the distance between two defects is fixed only by the fiber radius. The number  $1/\sqrt[4]{5}$  arises due to the fiber geometry. In the rectangular geometry this factor is 0.5, but in the circular domain it is 0.66. Generalization of this analysis to other fiber geometries of industrial relevance, such as elliptical, is possible. Next we shall establish the accuracy and relevance of the theoretical results by comparing numerical solutions of the full non-linear system of parabolic partial differential equations (21) with the theoretical prediction given by Eq. (45).

## 4. Modeling fiber texture structure

### 4.1. Computational modeling

The model equation (21) is a set of five coupled non-linear parabolic partial differential equations, solved in a circle, subject to the auxiliary conditions (see Eqs. (25) and (28)). The equations are solved using Galerkin Finite Elements with Lagrangean linear basis functions for spatial discretization and a fifth-order Runge–Kutta–Cash–Karp time adaptive method. Since we use Galerkin Finite Elements, the boundary conditions are exactly satisfied,

and  $\mathbf{Q}$  at the surface ( $\tilde{r} = 1/2$ ) is exactly equal to  $\mathbf{Q}_o$  (see Eq. (20)). Convergence and mesh independence were established in all cases. Convergence spatial discretization was judiciously selected taking into account the length scale of our model. As mentioned above, the Landau–de Gennes model for nematic liquid crystals has an external length scale  $L_e$  and an internal length scale  $r_c$  as follows:

$$L_e = R \quad (46a)$$

$$r_c = \xi = \sqrt{\frac{L_1}{ckT^*}} \quad (46b)$$

where  $R$  is the fiber radius, and  $r_c = \xi$  is the defect core size introduced in Section 3. For typical liquid crystals the defect core size is in the molecular size range [6], and its characteristic size (radius) is given by the square root of the ratio of the characteristic long-range energy ( $L_1$ ) density and the characteristic short-range energy ( $ckT^*$ ). The length scale obeys  $L_e = R \gg r_c$  [6]. To find a numerical value for  $r_c$ , the Landau bare elasticity modulus  $L_1$  and the thermal energy factor  $ckT^*$  are needed. The Landau bare elasticity modulus  $L_1$  [4] has been measured for many liquid crystalline materials [6], while the value for  $ckT^*$  is found from the isotropic–nematic phase transition temperature  $T^*$  [4]. If defects are present, the mesh size has to be smaller than  $r_c$ , which produces severe computational problems. The computational problem arising from disparate length scales ( $L_e = R \gg r_c$ ) is a topic of current research and is far from solved. It should be noted that the external length scale governs the directors' orientation ( $\mathbf{n}, \mathbf{m}, \mathbf{l}$ ) while the internal length scale governs the scalar order parameter ( $S, P$ ). In addition, care should be taken to select an appropriate time integration technique to overcome the intrinsic stiffness of the system. The model equations contain an internal time scale  $\tau_i$  and an external time scale  $\tau_e$ . The internal time scale governs the evolution of the scalar order parameters ( $S, P$ ) and is given by

$$\tau_i = \frac{\eta}{ckT^*} \quad (47)$$

A much longer external time scale  $\tau_e$  controls the evolution of the directors and is given by

$$\tau_e = \frac{\eta L_e^2}{L_1} \quad (48)$$

The selected adaptive time integration scheme is able to efficiently take into account the stiffness that arises due to the disparity between time scales:  $\tau_i \ll \tau_e$ .

### 4.2. Results and discussion

To efficiently visualize the solution vector  $\mathbf{Q}$ , we represent  $\mathbf{Q}$  by a cuboid whose axes are the directors ( $\mathbf{n}, \mathbf{m}, \mathbf{l}$ ) and whose axes are proportional to its eigenvalues. Since  $\mathbf{Q}$  has negative eigenvalues, we visualize  $\mathbf{M} = \mathbf{Q} + \frac{1}{3}\mathbf{I}$  instead of  $\mathbf{Q}$ .

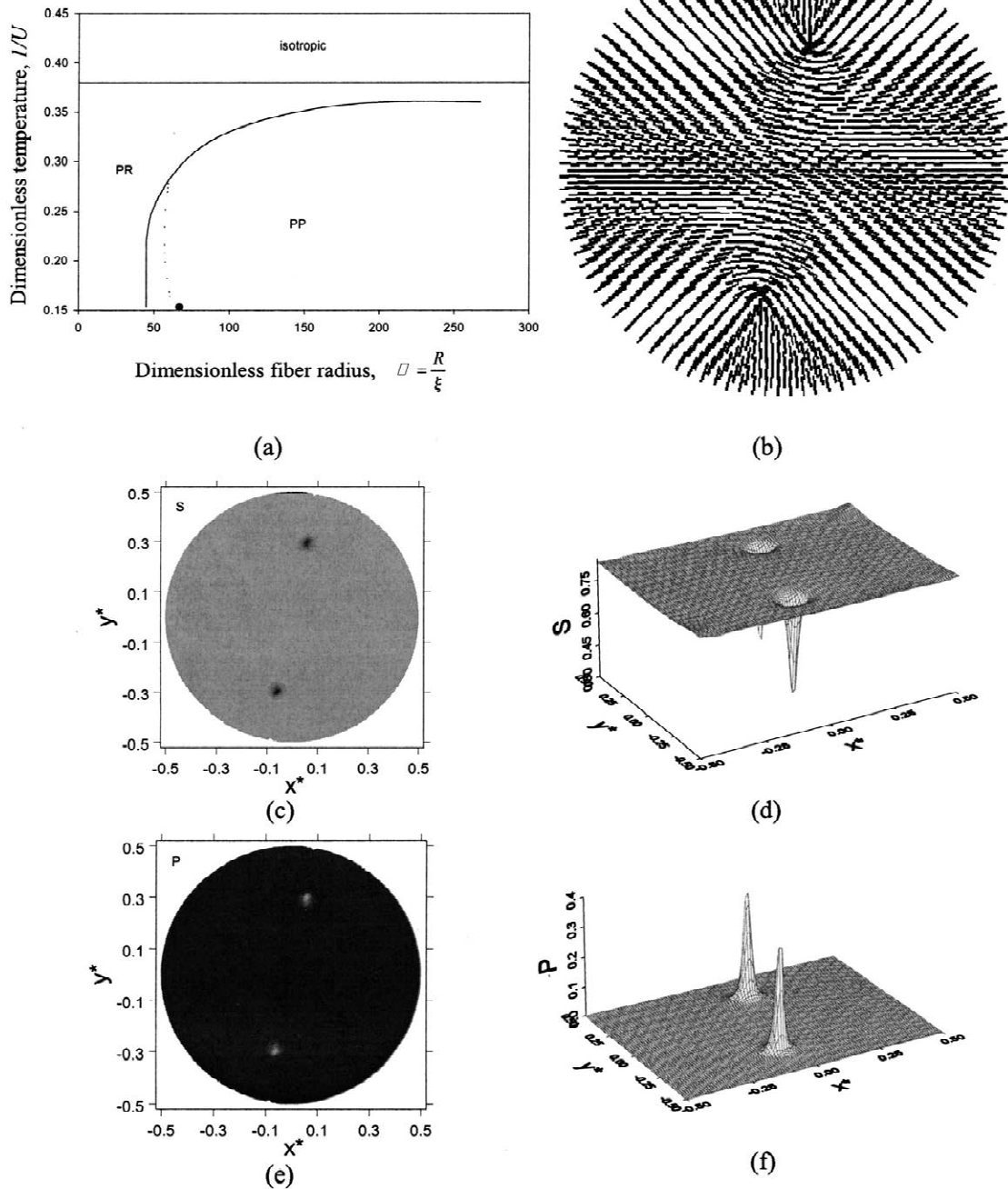


Fig. 5. (a) Computed texture phase diagram, given in terms of nematic potential  $1/U = T/3T^*$  as a function of dimensionless fiber radius  $\Psi = R/\xi$  for the auxiliary conditions (Eqs. (20) and (28),  $2.8 \leq U \leq 6.55$ ,  $0 < \Psi < 150$ ). (b) Steady-state solution of the planar polar texture for  $U = 6.55$ ,  $R = 67$ ,  $\tilde{L}_2 = -0.5$ . (c,d) Gray-scale plot and surface plot of the uniaxial scalar order parameter  $S$  as a function of dimensionless distance  $(x^*, y^*)$ . In the gray-scale plot the low order parameter ( $S \approx 0$ ) is black and the high order parameter ( $S \approx 1$ ) is white. The dark dots in the figure correspond to the two  $s = +1/2$  defects. The narrow peaks in the surface plots indicate the difference in scale between defect cores and fiber radius. At the defects' core  $S < S_{eq}$ , as expected. (e,f) Gray-scale and surface plots of the biaxial order parameters  $P$  as a function of dimensionless distance  $(x^*, y^*)$ . In the gray-scale plot,  $P \approx 0$  corresponds to black and  $P \approx 1$  to white. The figure clearly shows that  $P > 0$  at the two defect cores. The corresponding surface plot shows that, at the defects' core,  $P \approx 0.4$  and strong biaxiality is present.

Fig. 5a shows the computed texture phase diagram, given in terms of nematic potential  $1/U = T/3T^*$  as a function of dimensionless fiber radius  $\Psi = R/\xi$  for the auxiliary conditions (25) and (28), and  $2.8 \leq U \leq 6.55$ ,  $0 < \Psi < 150$ . The phase diagram identifies the stability of the textures as a function of temperature and fiber radius. An ultra-thin fiber favors the PR texture while lower temperature and thicker fiber favors the stability of the PP texture. The full curved line indicates the PP and PR transition line. The area between the full curved and dashed line shows bistability. This is due to the lack of numerical resolution beyond our available computational power. In this area, either of the PR and PP textures were obtained. The dot near the bottom of the diagram represents the parametric conditions used in obtaining Fig. 5b. For  $U > 8/3$ , the fiber is isotropic. The phase diagram shows that the processing (temperature) and geometry (fiber radius) affect the texture selection process. Fig. 5b is a representative typical steady-state solution of the planar polar texture for  $U = 6.55$ ,  $\Psi = 67$ ,  $\tilde{L}_2 = -0.5$ . It clearly shows the characteristic planar polar texture, with the two  $s = +1/2$  defects collinear with the fiber axis; at the boundary  $\mathbf{Q}$  satisfies the boundary condition (25). Since  $\mathbf{Q}(x, y, t)$  the solutions are invariant along the fiber axis. The orientation of the defect–defect axis is arbitrary since the system evolves from an isotropic state that contains no texture information. The simulations show the bending distortions close to the two defects and an aligned region between the two defects. Fig. 5c and d show a gray-scale plot and a surface plot of the uniaxial scalar order parameter  $S$  as a function of dimensionless distance  $(x^*, y^*)$ . In the gray-scale plot the low order parameter ( $S \approx 0$ ) is black and the high order parameter ( $S = 1$ ) is white. The boundary of the scalar order parameter is exactly equal to the equilibrium value  $S_{eq} = 0.827$  obtained from Eq. (17) when  $U = 6.55$ . The dark dots in the figure correspond to the two  $s = +1/2$  defects. The narrow peaks in the surface plots indicate the difference in scale between defect cores and fiber radius. At the defects' core  $S \approx 0$ , as expected. Fig. 5e and f show the corresponding gray-scale and surface plots of the biaxial order parameters  $P$  as a function of dimensionless distance  $(x^*, y^*)$ . In the gray-scale plot,  $P \approx 0$  corresponds to black and  $P \approx 1$  to white. The figure clearly shows the biaxial eigenvalue of  $\mathbf{Q}$  at the two defect cores. The corresponding surface plot shows that, at the defects' core,  $P \approx 0.4$  and strong biaxiality is present. The reason why  $s = +1/2$  defects show biaxial ordering is because this class of defect ( $|s| = \frac{1}{2}$ ) lacks cylindrical symmetry and hence  $P$  must be non-zero.

Fig. 6a–d show a computed visualization of the evolution of the tensor order parameters  $\mathbf{Q}$  for the same parametric conditions as in Fig. 5, for the following dimensionless times: (a) 200, (b) 400, (c) 800, (d) steady state. The figure shows that, at early times, the texture is close to the PR texture with the two defects close to the fiber axis, and as time proceeds the defects move away

from each other and towards the fiber surface. The reason for the increase in the defect–defect distance is the mutual and equal repulsive force between two defects of equal sign and strength, which in this case is  $+1/2$ . The defects drift apart and eventually slow down and settle at a distance  $x$  from the fiber axis, because of the repulsive image forces arising from the fixed boundary conditions (Eq. (17)). Fig. 6e shows the corresponding total dimensionless long-range energy  $f_1^*$  as a function of dimensionless time  $t^*$ . The total dimensionless long-range energy  $f_1^*$  is obtained by integrating Eq. (13b):

$$f_1^* = \frac{\xi^2}{2R^2} \int_A \{ \tilde{\nabla} \mathbf{Q} : (\nabla \mathbf{Q})^T + \tilde{L}_2 (\tilde{\nabla} \cdot \mathbf{Q}) \cdot (\tilde{\nabla} \cdot \mathbf{Q}) \} dA \quad (49)$$

where  $A$  is the computational domain, and the dimensionless time is given by

$$t^* = t \frac{3ckT^*}{\eta} \quad (50)$$

Fig. 6e shows that the long-range energy decreases non-monotonically with time. The increase in  $f_1^*$  at  $t^* = 180$  indicates the following topological transformation:

$$s_1 \rightarrow 2s_2 \quad (51)$$

where  $s_1 = +1$  and  $s_2 = +1/2$ . The driving force to this transformation is the reduction of the long-range elastic energy. The long-range elastic energy associated with a defect scales with the square of its strength and, since  $(s_1)^2 > 2(s_2)^2$ , the emergence of two  $s = +1/2$  defects lowers the energy. The local maximum in  $f_1^*$  indicates the global dimensionless time  $t^*$  at which the defect transformation (Eq. (51)) occurs. Fig. 6f shows the corresponding dimensionless defect separation distance  $d^*$  as a function of dimensionless time  $t^*$ . The horizontal line corresponds to the theoretical results derived in the previous section:  $d^* = x/R = 1/\sqrt[4]{5}$  (see Eq. (45)). The figure clearly shows that, as  $t^*$  increases, the defect–defect separation distance increases and eventually asymptotes to the predicted value of  $1/\sqrt[4]{5}$ .

Fig. 7 shows the dimensionless defect separation distance  $d^*$  as a function of dimensionless temperature  $T/3T^*$ , for  $Y = 67$ , and the dimensionless defect separation distance  $d^*$  as a function of dimensionless fiber radius  $\Psi = R/\xi$ , for  $U = 3.55$ . The solid line corresponds to the theoretical result,  $d^* = 1/\sqrt[4]{5}$ . The results confirm the validity of Eq. (45). It should be mentioned that deviations from the theoretical result are likely to originate from computational limitations that arise due to the inherent disparate length scales in the model. Also, for the presented results and parametric conditions, anisotropic Frank elasticity has no effect on  $x$ . Nevertheless, we expect that, for higher  $U$ , the magnitude of  $\tilde{L}_2$  will affect the ideal value of  $x = 1/\sqrt[4]{5}R$ .

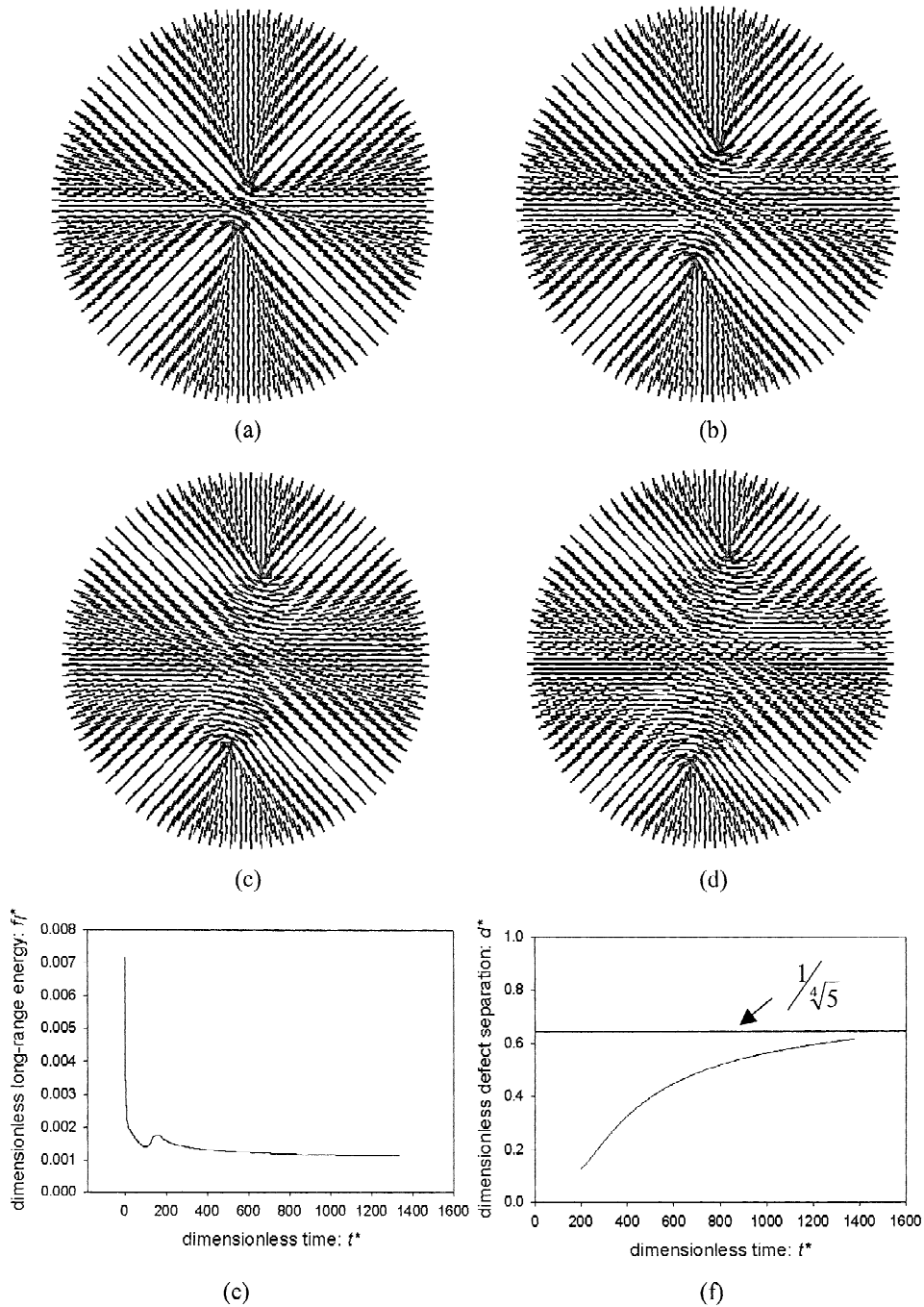


Fig. 6. (a–d) Computed visualization of the evolution of the tensor order parameters  $Q$  for the same parametric conditions as in Fig. 5. (e) Total dimensionless long-range energy  $f_1^*$  as a function of dimensionless time  $t^*$ . The long-range energy decreases non-monotonically with time. The increase in  $f_1^*$  at  $t^* = 180$  indicates the topological transformation  $s_1 \rightarrow 2s_2$ . (f) Dimensionless defect separation distance  $d^*$  as a function of dimensionless time  $t^*$ . The horizontal line corresponds to the theoretical results derived in the previous section:  $d^* = x/R = 1/\sqrt[4]{5}$ . Parametric conditions:  $U = 6.55$ ,  $\Psi = 67$ ,  $\tilde{L}_2 = -0.5$ .

## 5. Conclusion

A model to describe texture formation in mesophase carbon fibers has been developed, implemented, and shown

to replicate commonly observed cross-sectional carbon fiber textures of industrial relevance. The model is based on the classical Landau–de Gennes theory for liquid crystals and has been adapted to describe discotic mesoph-

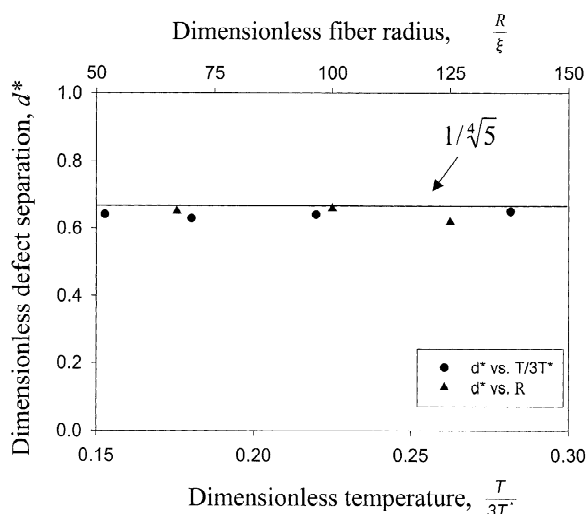


Fig. 7. The dimensionless defect separation distance  $d^*$  as a function of dimensionless temperature  $T/3T^*$ , for  $\Psi = 67$  (lower scale), and dimensionless defect separation distance  $d^*$  as a function of dimensionless fiber radius  $\Psi = R/\xi$ , for  $U = 3.55$  (top scale). The solid line corresponds to the theoretical result,  $d^* = 1/\sqrt{5}$ .

ases. The model is able to predict the formation of planar radial and planar polar textures. The parametric envelope of their stability in terms of temperature and fiber radius has been computed. Lower temperature and thicker fiber tend to select the planar polar texture and higher temperature and thin fiber tend to promote the emergence of the planar radial texture. A geometric analysis of the planar polar texture has been performed and the defect separation distance is shown to be equal to  $1/\sqrt{5}$ . Computational modeling of texture formation shows that the two defects in the planar polar texture arise from a topological transformation that involves the decay of a  $+1$  defect into two  $+1/2$  defects. The numerical results show that the computed defect separation distance equations with the theoretical results for different fiber radius and temperatures. The new results presented in this paper contribute towards a better understanding of the principles that control cross-section texture selection during the melt spinning of carbonaceous mesophases.

## 6. Uncited references

[8]; [9]

## Acknowledgements

This research was supported in part by a grant from the Donors of The Petroleum Research Fund (PRF) administered by the American Chemical Society, and in part by the ERC Program of the National Science Foundation under Award Number EEC-9731680.

## References

- [1] Riggs DM, Shuford RJ, Lewis RW. Graphite fibers and composites. In: Lubin G, editor. Handbook of composites. New York: Van Nostrand Reinhold, 1982, pp. 196–271.
- [2] Hurt RH, Chen ZY. Phys Today 2000;53(3):39–59.
- [3] Peebles Jr. LH. Carbon fibers—formation, structure, and properties. Boca Raton, FL: CRC Press, 1995.
- [4] McHugh JJ, Edie DD. Carbon 1996;34(1):1315–22.
- [5] McHugh JJ, Edie DD. Liquid Crystals 1995;18(2):327–35.
- [6] de Gennes PG, Prost J. The physics of liquid crystals, 2nd ed.. Oxford: Clarendon Press, 1993.
- [7] Sokalski K, Ruijgrok TW. Physica 1982;113A:126–32.
- [8] Wang L, Rey AD. Modeling Simul Mater Sci Eng 1997;5:67–77.
- [9] Sonnet A, Kilian A, Hess S. Phys Rev E 1995;52:718–22.
- [10] Tsuji T, Rey AD. J Non-Newtonian Fluid Mech 1997;73:127–52.
- [11] Longa L, Monselesan D, Trebin HR. Liquid Crystals 1987;2(6):769.
- [12] Singh AP. Modelling and simulation of morphological phenomena in discotic mesophases. PhD Thesis. Montreal, Quebec, Canada: McGill University, 2000.
- [13] Beris AN, Edwards BJ. Thermodynamics of flowing systems. Oxford: Clarendon, 1994.
- [14] Doi M, Edwards BJ. The theory of polymer dynamics. Oxford: Clarendon, 1986.
- [15] Rey AD, Denn MM. Annu Rev Fluid Mech 2002;34:233–65.
- [16] Rey AD. Phys Rev E 2000;61:1540–9.